

A spatial correlation technique for estimating velocity fields using molecular tagging velocimetry (MTV)

C. P. Gendrich, M. M. Koochesfahani

67

Abstract A direct spatial image correlation technique is presented for estimating the Lagrangian displacement vector from image pairs based on molecular tagging diagnostics. The procedure provides significant improvement in measurement accuracy compared to existing approaches for molecular tagging velocimetry (MTV) analysis. Furthermore, this technique is of more general utility in that it is able to accommodate other laser tagging patterns besides the usual grid arrangement. Simulations are performed to determine the effects of many experimental and processing issues on the sub-pixel accuracy of displacement estimates. The results provide guidelines for optimizing the implementation of MTV. Experimental data in support of this processing technique are provided.

1 Introduction

The use of molecular tagging diagnostics for flow studies has received increasing attention over the last decade. Molecular tagging velocimetry (MTV), in particular, takes advantage of molecules premixed in the flowing medium that can be turned into long lifetime tracers upon excitation by photons. A pulsed laser is typically used to tag the regions of interest. The luminescence from the tagged regions is imaged at two successive instances within the tracer's lifetime. The measured Lagrangian displacement vector provides the estimate of the velocity vector. To measure two components of the velocity in a plane, the luminescence intensity field must have spatial gradients along two, preferably orthogonal, directions. For single-point velocimetry, this is easily achieved using a pair of crossing laser beams; a grid of intersecting laser lines allows multipoint velocity measurement. An example is illustrated in Fig. 1.

Past implementations of this velocimetry approach include the use of photochromic molecules (LIPA, Falco and Chu 1987, Chu et al. 1993), excited-state oxygen fluorescence (RELIEF, Miles et al. 1987), specially engineered water-soluble phosphorescent molecules (Koochesfahani et al. 1993, Hill and Klewicki 1994, Stier 1994, Gendrich et al. 1994), and caged fluorescein (PHANTOMM, Lempert et al. 1995). A review of other efforts to measure flow velocities using molecular tagging can be found in Falco and Nocera (1993). In the works of Miles et al. and Lempert et al., laser line tagging is used (i.e., not grids), and the velocity is inferred from the displacement of the line centers. Clearly this type of tagging can provide only one component of the velocity, that normal to the tagged line. In addition, there is an inherent error associated with this velocity component estimate (see Hill and Klewicki 1996, Koochesfahani et al. 1996). In all other implementations using laser grid tagging (except for the work from our laboratory), the displacement of the grid intersections is also determined by locating the centers of the laser lines using various techniques. The highest level of accuracy achieved to date in determining the displacement vector by this approach has been reported by Hill and Klewicki (1996) to be ± 0.35 pixel RMS.

It is desirable to determine the displacement vector with the highest possible sub-pixel accuracy in order to increase the dynamic range of the velocity measurements and to improve the accuracy of vorticity estimates. In addition, for a given required dynamic range, a higher sub-pixel accuracy will allow a shorter time delay to be used between the two images, affording this technique a higher bandwidth in measuring unsteady flow phenomena.

In this paper we present a spatial image correlation technique for estimating the displacement vector of the tagged regions with a much higher level of accuracy than what has been achieved previously. Typical improvements by an order of magnitude are reported. Furthermore, this technique is of more general utility in that it is able to accommodate other laser tagging patterns besides grids. The implementation of the spatial correlation technique is first described, followed by an analysis of the effects of various experimental and analysis parameters on the accuracy of the displacement estimates. The results are based on computer simulations and subsequently verified using experimental data.

2 Spatial correlation technique

Consider a region in a flow tagged at time t_1 by an intersecting pair of laser beams as shown in Fig. 2a. This would correspond

Received: 25 January 1996/Accepted: 6 May 1996

C. P. Gendrich, M. M. Koochesfahani
Department of Mechanical Engineering,
Michigan State University, East Lansing, MI 48824, USA

Correspondence to: C. P. Gendrich

This work was supported by the Air Force Office of Scientific Research under grants F49620-92-J-0338 and F49620-95-1-0391. This work made use of MRSEC shared facilities supported by the National Science Foundation Award Number DMR-9400417. The authors would also like to thank Richard Cohn for his assistance in preparing the manuscript.

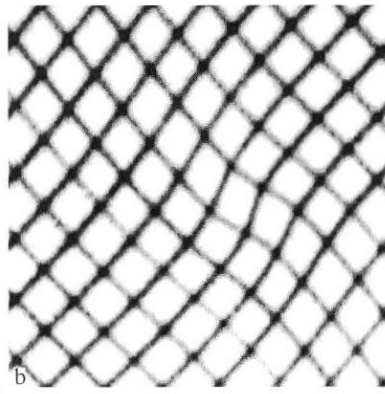
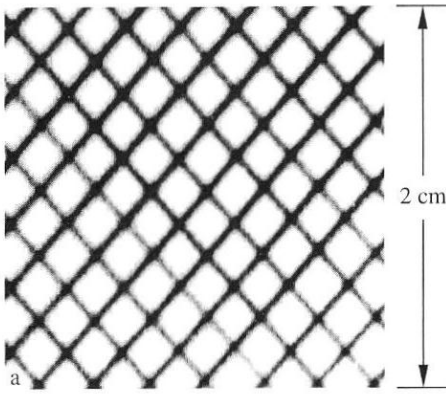


Fig. 1a,b. Sample experimental MTV grid. a just after laser tagging; b displaced grid 6 ms later

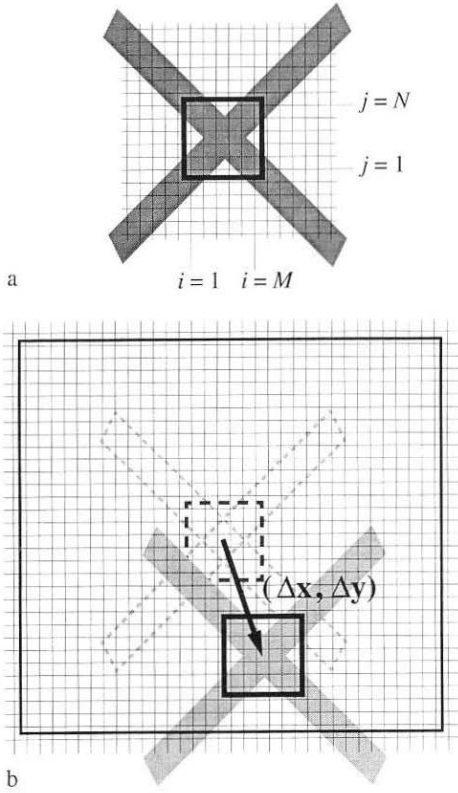


Fig. 2a,b. Spatial correlation technique schematic. a Tagged region at time $t=t_1$; black border highlights the source window; b tagged region displaced by $(\Delta x, \Delta y)$ at time $t_2=t_1+\Delta t$; dashed lines indicate the original location of the region, large box depicts the roam window

to one of the grid intersections in Fig. 1. The tagged region is displaced by an amount $(\Delta x, \Delta y)$ to a new location at a later time $t_2=t_1+\Delta t$ as a result of the local flow velocity, Fig. 2b. A small window, referred to as the source window, is selected about the tagged region in the earlier image, and it is spatially correlated with a larger roam window in the second image. The roam window is centered about the original location of the source window, and its extent is large enough to encompass the displacement vector. We calculate the spatial correlation coefficient $R(r, s)$ between the intensity field I_1 of the source window and I_2 of the roam window as a function of the pixel

displacement (r, s) between them. The location of the peak in $R(r, s)$ defines the displacement vector accurate to within one pixel. Sub-pixel accuracy is obtained using a two-dimensional polynomial fit, the details of which will be discussed later. The correlation coefficient is computed according to:

$$R(r, s) = \frac{\overline{I_1 \cdot I_2} - \overline{I_1} \cdot \overline{I_2}}{\sigma_{I_1} \cdot \sigma_{I_2}}$$

In this expression, the overbar refers to the expected value, and σ denotes the standard deviation. With this definition, $-1 \leq R \leq +1$. The representation of the various terms shown above in terms of the image pixel values are:

$$\overline{I_1 \cdot I_2} = \frac{1}{M \cdot N} \sum_{i,k} \sum_{j,l} I_1(i, j) \cdot I_2(k, l) \quad \begin{cases} i = [1, \dots, M] \\ j = [1, \dots, N] \\ k = [1+r, \dots, M+r] \\ l = [1+s, \dots, N+s] \end{cases}$$

$$\overline{I_1} = \frac{1}{M \cdot N} \sum_i \sum_j I_1(i, j) \quad \begin{cases} i = [1, \dots, M] \\ j = [1, \dots, N] \end{cases}$$

$$\overline{I_2} = \frac{1}{M \cdot N} \sum_k \sum_l I_2(k, l) \quad \begin{cases} k = [1+r, \dots, M+r] \\ l = [1+s, \dots, N+s] \end{cases}$$

$$\sigma_{I_1} = \sqrt{\frac{1}{M \cdot N} \sum_i \sum_j (I_1(i, j) - \overline{I_1})^2} \quad \begin{cases} i = [1, \dots, M] \\ j = [1, \dots, N] \end{cases}$$

$$\sigma_{I_2} = \sqrt{\frac{1}{M \cdot N} \sum_k \sum_l (I_2(k, l) - \overline{I_2})^2} \quad \begin{cases} k = [1+r, \dots, M+r] \\ l = [1+s, \dots, N+s] \end{cases}$$

We typically employ square windows (i.e., $M=N$) and do not compute over the entire roam window domain when prior information is available regarding the approximate location of the displacement vector. It should be noted that the procedure described above can also be applied to process digital particle image velocimetry (DPIV) image pairs; see for example Fincham and Spedding (1995) and Roesgen and Totaro (1995). Our procedure is, however, different from the image cross correlation procedure suggested by Utami et al. (1991), and Keane and Adrian (1992) where only the direct cross correlation $\overline{I_1 \cdot I_2}$ is computed instead of the complete correlation coefficient $R(r, s)$ defined earlier.

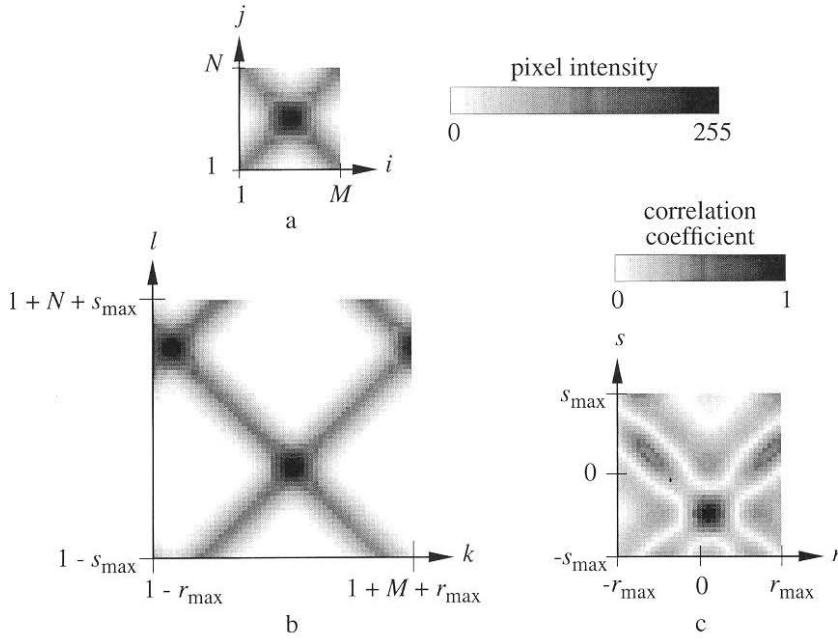


Fig. 3a–c. Simulated single grid intersection. a Source window; $M=N=21$ pixels; b roam window; c correlation coefficient field; $r_{\max}=s_{\max}=15$ pixels

The computed displacement vector is used to estimate the spatial average of the velocity within the source window according to $(u, v) = (\Delta x / \Delta t, \Delta y / \Delta t)$. It is understood that Δt must be short enough to minimize image distortion due to velocity gradients (i.e., strain rate and vorticity). Higher order procedures to take these effects into account as introduced by Huang et al. (1993), Maas et al. (1994), and Tokumaru and Dimotakis (1995) could also be applied here. Furthermore, the maximum displacement is usually kept to less than one half of the grid spacing in order to guard against spurious correlation with other grid nodes. The latter restriction can be relaxed using a variety of techniques including grid lines with different intensities.

An example illustrating the application of the spatial correlation approach is shown in Fig. 3. The source window from a computer-simulated laser grid intersection is depicted in Fig. 3a; the roam window from the corresponding simulated image displaced by $(\Delta x, \Delta y) = (2.1, -8.5)$ is indicated in Fig. 3b. The correlation coefficient field, Fig. 3c, exhibits a well-defined peak of near unity value. A seventh-order two-dimensional polynomial fit of a 9×9 pixel region about the correlation peak yields a displacement estimate accurate to 0.013 pixel.

As might be expected, the accuracy of a displacement measurement is influenced by many factors such as signal-to-noise ratio (S/N) in the image pairs, image contrast, laser grid crossing angle θ , the order of the polynomial fit for sub-pixel estimation of displacement, etc. These and other effects are addressed in this paper using computer simulations.

3 Simulation parameters

An image, representing a region of the flow tagged at the initial time $t = t_1$, is simulated by laying down a 10×10 grid of lines with a known laser line intensity profile and intersecting at a prescribed angle. For most cases a Gaussian laser line profile

with a full-width ($1/e^2$ point) of $W=11$ pixels is used. Results based on a non-Gaussian profile, corresponding to the excimer lasers we employ for our experiments, and other laser line widths are obtained also. The image is represented by an 8-bit intensity range typical of those produced by most digital image acquisition systems to date.

A second image, representing the tagged region at the later time $t_2 = t_1 + \Delta t$, is computed by displacing the grid lines of the original image according to a prescribed displacement vector (not necessarily an integral number of pixels). As mentioned earlier, the maximum displacement is kept to less than half of the grid spacing. The contrast and S/N of the second image are adjusted in the following manner: First the pixel intensities are scaled to achieve the desired contrast, defined to be the difference between the brightest and darkest pixels in the image. Noise uniformly distributed over a range $(-n, +n)$ is then added to each pixel, where n represents the maximum noise level. We define the S/N of these noisy images as contrast over peak-to-peak noise level (i.e., $2n$). If a pixel's value, after adding noise, exceeds the limiting values 0 or 255, it is set equal to the corresponding limit.

It should be noted that the “earlier” images always had the highest possible contrast of 255 and the greatest signal to noise for an 8-bit image (i.e., $S/N=255$ corresponding to ± 0.5 pixel discretization). This ideal can actually be approached in our experiments, because the earlier images are acquired very shortly after each laser pulse, before the luminescence intensity of our phosphorescent tracer has decayed appreciably. It is the second image, acquired later in the luminescence process, which suffers from degraded S/N , the image degradation being connected to the time delay between the laser tagging pulse and the image interrogation. An example of simulated noisy images is shown in Fig. 4. An S/N value between 4 and 8 is typical of our second images.

Our simulations, for each set of parameters (e.g., S/N , intersection angle, etc.), consider 100 image pairs corresponding

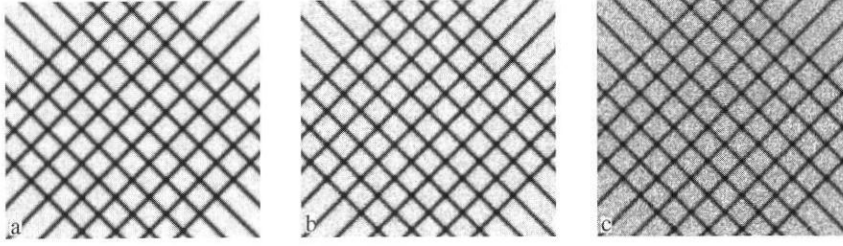


Fig. 4a–c. Examples of simulated grid patterns.
a $S/N=8$; b $S/N=4$; c $S/N=2$

to 100 different displacement vectors between the two. Each image contains anywhere from 44 to 100 grid intersections, the actual number depending on the grid intersection angle. Each simulation, therefore, considers the comparison between the estimated and actual displacement for a total of 4400 to 10000 vectors. All of the computed displacement vectors are used for the analysis, regardless of the magnitude of the correlation peak. The error in the estimated displacement is referred to as $\delta x = (\Delta x)_{\text{estimated}} - (\Delta x)_{\text{actual}}$, and $\delta y = (\Delta y)_{\text{estimated}} - (\Delta y)_{\text{actual}}$, so the magnitude of the displacement error $\delta q \equiv [(\delta x)^2 + (\delta y)^2]^{1/2}$ gives an indication of the overall measurement uncertainty. A fixed source window size of 21×21 pixels is used throughout except for when the effect of window size is specifically being addressed: see Sect. 7. It should be noted, as indicated earlier, that these simulations address accuracy issues associated with a first order linear displacement estimate, which is clearly appropriate for flow fields where the velocity gradients within the source window are small.

The cumulative probability distribution function of the displacement error δq is constructed, and the value of δq corresponding to the 95% confidence interval, $(\delta q)_{0.95}$, is used throughout this paper as the quoted measure of uncertainty. This implies that 95% of the computed displacements have errors less than or equal to $(\delta q)_{0.95}$. Note that this is a more conservative estimate of measurement error than the RMS value. If the error distribution is Gaussian, then the RMS error estimate is $(\delta q)_{\text{RMS}} = 0.5(\delta q)_{0.95}$.

4

Effects of signal to noise ratio and intersection angle

The results described in this section are based on a series of simulations in which the S/N is varied from 1 to 255; the contrast of the second image before adding noise is 104 in all cases. This value of contrast is typical of our experimental data; the results for other contrast values will be discussed in Sect. 6. The intersection angle θ between the laser lines ranges from 90° to 150° . This angle is typically dictated by the flow facility and optical access restrictions in an experiment. A seventh-order two-dimensional polynomial fit of a 9×9 pixel region about the correlation peak is used to estimate the displacement with sub-pixel accuracy. This choice of the fit is found to be optimum for most cases, see Sect. 5.

Figure 5 illustrates the displacement uncertainty $(\delta q)_{0.95}$ for different values of intersection angle and S/N . Note that the accuracy is relatively insensitive to the intersection angle up to $\theta = 130^\circ$ for all values of S/N shown. Except for the most extreme intersection angle of 150° , sub-pixel accuracy of 0.1 or better is obtained for S/N higher than 4 regardless of the intersection angle. The sub-pixel accuracy is 0.021 for $S/N=15$

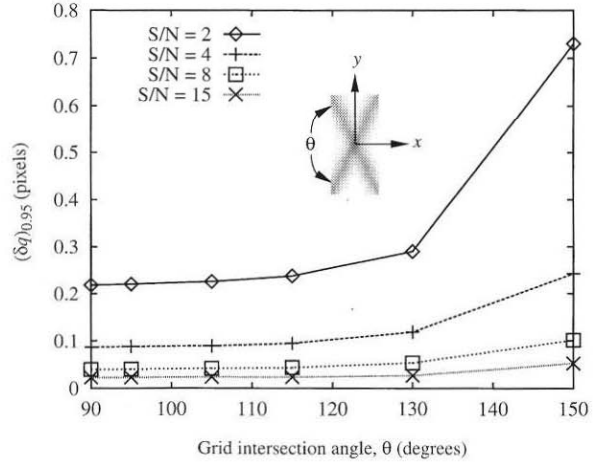


Fig. 5. Displacement sub-pixel accuracy versus θ for different values of S/N

and approaches a value of about 0.015 for higher values of S/N (not shown here).

The results shown in Fig. 5 address only the magnitude of the error vector. The errors in the estimated x - and y -components of the displacement vector (δx and δy) are in general not equal and depend on the intersection angle. For $\theta = 90^\circ$ the error magnitudes $|\delta x|$ and $|\delta y|$ are comparable; however, as the intersection angle increases, $|\delta x|$ values decrease at the expense of increasing $|\delta y|$. As expected, in the limit of $\theta = 180^\circ$ the determination of Δy becomes ill-posed. As with δq , we can characterize the uncertainty in the two displacement components in terms of their respective 95% confidence interval estimates $|\delta x|_{0.95}$ and $|\delta y|_{0.95}$. The behavior of the ratio of these estimates, shown in Fig. 6, highlights the effect just described.

According to Fig. 6, the error in displacement Δy relative to Δx (hence the error in the v -component velocity estimate relative to the u -component) monotonically increases with increasing intersection angle. For example, at $\theta = 130^\circ$ the error in the y displacement is expected to be twice that for the x displacement. The behavior is mostly insensitive to S/N for the range of values considered here.

Based on the results presented in this section, using intersection angles less than 130° and image S/N better than 4 should produce displacement estimates with better than 0.1 pixel accuracy in both the x - and y -directions. The accuracy improves with higher S/N images in the manner shown in Fig. 5.

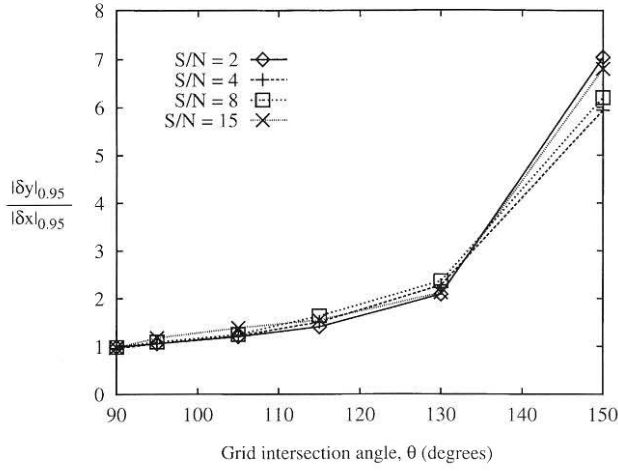


Fig. 6. Effect of intersection angle and S/N on the ratio of x - and y -displacement error magnitudes

5 Effects of the fitting polynomial order

The fit function used to determine the displacement to sub-pixel accuracy must be able to model asymmetric correlation coefficient fields $R(r, s)$, which may be highly distorted in some cases. An odd high-order polynomial can be used for this purpose; a two-dimensional polynomial $F(x, y)$ of order P described below is used in this work.

$$F(x, y) = \sum_{i=0}^P (c_{i,0} x^i y^0 + c_{i,1} x^{i-1} y^1 + \dots + c_{i,i} x^0 y^i)$$

Note that fitting a polynomial of order P requires the “best fit” determination of $\frac{1}{2}(P+1)(P+2)$ coefficients; this value also specifies the minimum number of data points needed from the correlation field. Since a $K \times K$ pixel square region about the correlation peak is used for the fit, a minimum size of this region is required to provide enough data points for calculating the fit coefficients. The sides of this square region are chosen to be an odd number of pixels long so that the region is symmetrically positioned relative to the correlation peak. For example, a seventh-order fit requires a minimum of 36 data points to determine its 36 coefficients. This means a fitted region with a minimum size of 7×7 pixels is required. A larger fitted region may improve the quality of the fit, as long as spurious correlations do not contaminate the additional data. The choice of the fit order and the size of the fitted region need to be optimized for the best sub-pixel accuracy at minimum computational cost.

In order to determine the optimal fit order and the size of the fitted region K , simulations are performed for a range of grid intersection angles (90° – 150°), S/N values (2–15), and image contrast levels (100–240). Results are shown in Fig. 7 in terms of the sub-pixel accuracy normalized by the minimum value that was achieved. This figure indicates an optimum choice of a seventh-order polynomial with a 9×9 pixel fitted region. This choice is found to be optimal for the entire range of the parameters considered, and it is used throughout this work. The actual minimum value of $(\delta q)_{\min}$ used in Fig. 7 depends upon the simulation parameters (see Fig. 5).

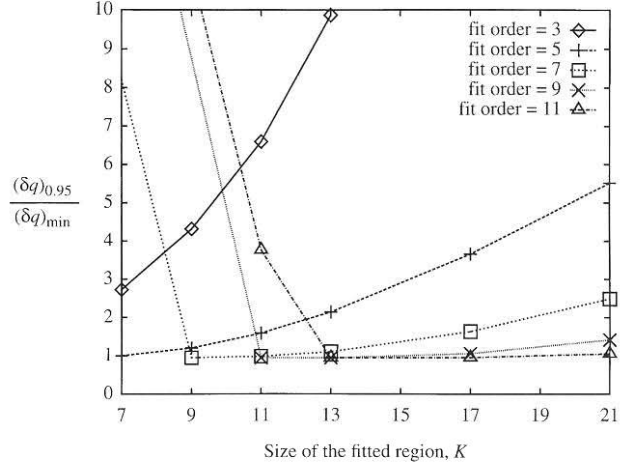


Fig. 7. Sub-pixel accuracy as a function of fit order and the size of the fitted region

6 Effects of image contrast level and image enhancement

As mentioned earlier, the second image is acquired later in the luminescence process, therefore it has a reduced contrast compared to the first image as a result of the exponentially decaying signal level. In this section, the effect of second image contrast on the accuracy of displacement estimates is addressed. Results are shown in Fig. 8 for a range of S/N values and grid intersection angles. Note that the results are given in terms of the ratio of $(\delta q)_{0.95}$ relative to the baseline case $(\delta q)_{\text{ref}}$ with a contrast level of 104, i.e., data in Fig. 5.

Figure 8 illustrates that as long as the contrast level is sufficiently high (52 in this case), the accuracy of the displacement measurement is quite insensitive to the actual contrast level, regardless of the S/N value. This relative insensitivity to the actual intensity range in the second image, i.e., I_2 in the equations in Sect. 2, might be expected, since scaling I_2 by a constant will not affect the values of the correlation

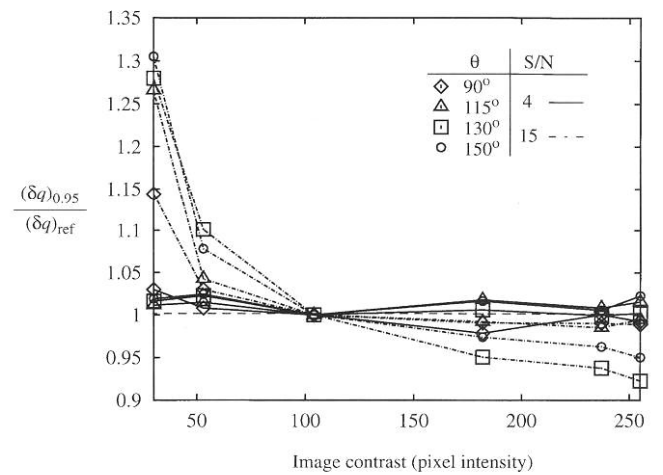


Fig. 8. Effects of image contrast on error magnitude for different grid intersection angles and S/N

coefficient $R(r, s)$. The practical implication of this result is that it is not necessary to boost the second image intensity by amplifying the detector output (assuming that it can be done without degrading S/N) beyond what is necessary to obtain a minimum contrast value.

For these same reasons, it was also expected that image enhancement by a linear contrast stretch would not improve the accuracy. To verify this, the second images in the simulations for Fig. 8 were linearly contrast stretched to the maximum of 255 and the results were recalculated. In all cases the accuracy decreased (by another 2%); this decrease is believed to be due to the additional noise generated in the re-discretization of the images.

7

Effects of laser line width and source window size

The displacement measured by the spatial correlation procedure is a spatial average over the source window domain. A smaller source window translates into improved spatial resolution. For a given grid line width, however, there may be an optimum source window size that yields the best sub-pixel accuracy in the measurement of the displacement. The optimum window size may also depend on the amount of noise present in the images. For example, a larger window size may counteract the impact of more noise due to its spatial averaging over a larger area. To investigate these issues, a series of simulations for a variety of laser (i.e., grid) line widths W , source window size L , and signal-to-noise ratios (S/N) are carried out.

The variation of sub-pixel accuracy $(\delta q)_{0.95}$ versus L/W is shown in Fig. 9a–d for four values of S/N and the particular

grid intersection angle $\theta = 90^\circ$, with lines of constant L and W indicated by the solid and dashed lines, respectively. Note that the particular values of $W = 11$, $L = 21$, and $L/W \cong 2$ have been used in the simulations discussed up to this point. In Fig. 9a we note that for a given line width W , if L/W is large enough the best sub-pixel accuracy is achieved. Using values of L/W larger than this will only degrade the measurement's spatial resolution (due to increasing L) without increasing its accuracy. For example, with $W = 17$ pixels, $L/W \cong 1.5$ is sufficient to give the best sub-pixel accuracy, and there is no need to use larger values of source window size L . Note that generally the optimum L/W falls in the range 1 to 3 for the values of W shown in Fig. 9a.

Figure 9a also illustrates that one cannot achieve the best absolute sub-pixel accuracy and the best spatial resolution (i.e., smallest source window size) simultaneously. For a given value of window size L , there is an optimum L/W (and hence line width W) for best accuracy. For example, with $L = 13$ pixels, $L/W \cong 1.5$ (and $W = 8.5$) corresponds to the lowest error; this accuracy is about 4 times worse than the best possible which can be achieved using a larger window size. The general observations made above also apply to the lower values of S/N shown in Fig. 9b–d, however, the optimum range of L/W tends to move to higher values as S/N decreases.

It is worth noting that good sub-pixel accuracy is still obtainable from very noisy images (Fig. 9d) for larger values of window size L and moderate grid line widths. As described earlier, this is due to the averaging effects in the correlation process. The trends for other grid intersection angles (not shown here) are similar to those discussed for $\theta = 90^\circ$, except the actual values of $(\delta q)_{0.95}$ increase as previously presented in Sect. 4.

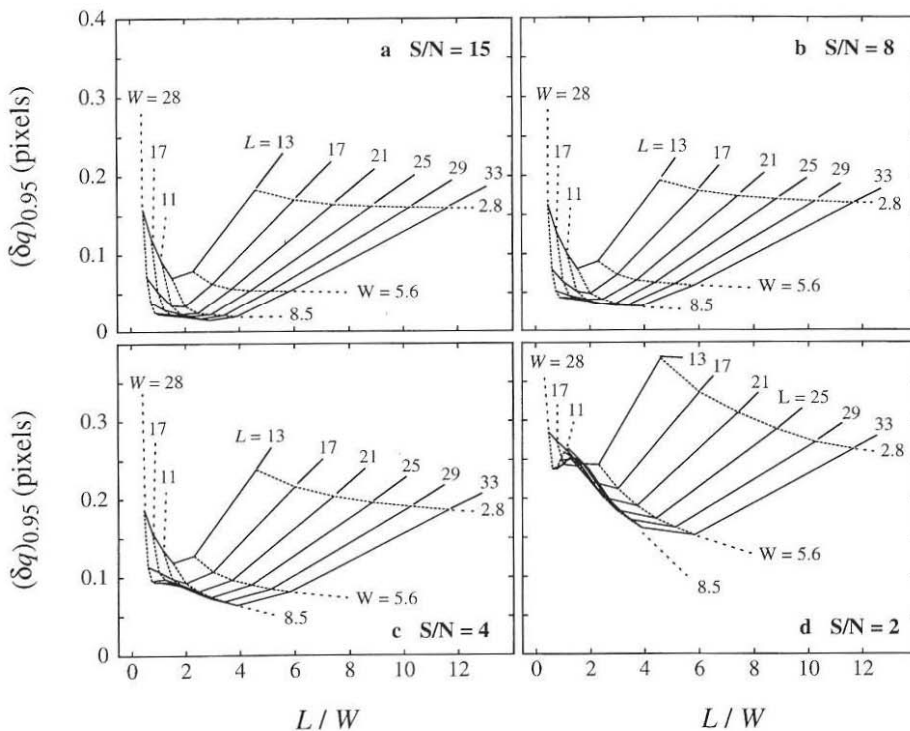


Fig. 9a–d. Error magnitude $(\delta q)_{0.95}$ as a function of laser line width W and source window size L for $\theta = 90^\circ$ and different values of S/N . Curves of constant L (solid lines) and W (dashed lines) are indicated

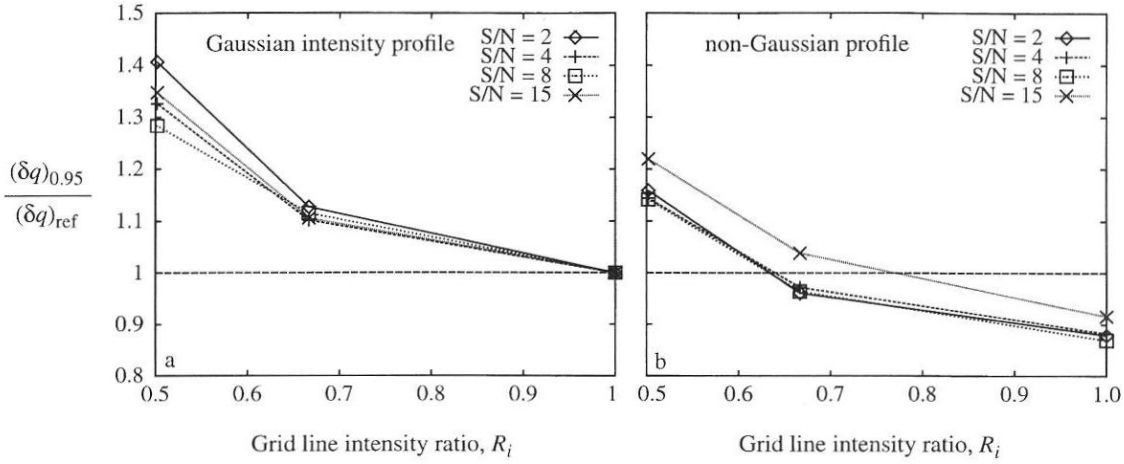


Fig. 10. Effects of grid line intensity ratio R_i on error magnitude $(\delta q)_{0.95}$ for $\theta = 90^\circ$

8

Other experimental concerns

Separate from the effects discussed so far, there are other issues related to the actual experimental implementation of the MTV approach which can influence the accuracy of the results. Specifically, we wish to discuss how accuracy is affected if the grid lines are not of equal intensity (e.g., due to unequal splitting of the laser beam or beam transmission problems), if the grid lines have a non-Gaussian intensity profile (e.g., use of excimer laser; see Sect. 10), or if images are sensed using interlaced instead of frame transfer detectors.

To address the effects of non-equal intensity grid lines, simulations are performed for intensity ratio R_i between the intersecting lines forming the grid varying between 1 (i.e., equal intensity) and 0.5. Non-Gaussian laser beams corresponding to that from an excimer laser are simulated using a flat top profile with rounded edges. The line width of the non-Gaussian profile is kept at 11 pixels for comparison with our baseline simulations which use an 11-pixel wide Gaussian profile.

The effect of intensity ratio R_i on the accuracy is shown in Fig. 10a for Gaussian and Fig. 10b for non-Gaussian intensity profiles for various values of S/N and the grid intersection angle $\theta = 90^\circ$. The effect is described in terms of the ratio $(\delta q)_{0.95}/(\delta q)_{\text{ref}}$ between the sub-pixel accuracy for the given R_i and that at $R_i = 1$ with Gaussian profile (i.e., $(\delta q)_{\text{ref}}$ is obtained from Fig. 5 using the appropriate S/N and $\theta = 90^\circ$). There are two main conclusions we wish to draw from Fig. 10. Regardless of the intensity profile there is little sensitivity to S/N , and there is a maximum of 40% reduction in accuracy for the lowest R_i and S/N considered. Interestingly, the non-Gaussian profile leads to better accuracy compared to Gaussian over the entire range of R_i .

In experimental implementations where interlaced detectors are used, each image contains every other horizontal line of the complete image. The complete image can then be formed by filling in the missing horizontal lines using interpolation. A simulation of images acquired in this manner reveals a degradation of up to 35–40% in sub-pixel accuracy compared to the full-frame images for the full range of S/N values and grid angles θ presented in this paper. As may be expected, this

degradation is mostly due to loss of accuracy in the component of displacement in the vertical direction. Therefore, interlaced cameras can be used with this accuracy reduction in mind.

9

Correlating other image features in the source window

It was mentioned earlier that the image within the source window must have sufficient intensity gradients in two preferably orthogonal directions to allow the determination of two components of velocity. These gradients have been created in the analyses above using a crossing grid pattern (i.e., an “X” pattern). Clearly any image pattern within a source window is likely to suffice, subject to this image intensity gradient requirement. For example the four corners of a grid intersection may be used for this purpose, see Fig. 11a. The advantages are an increased density of velocity vectors and the possibility of determining a more local estimate of the vorticity and strain rate based on the motion of an individual grid intersection (using the velocity of its four corners) instead of the motion of the larger grid box (using the velocity of its four grid intersections, Fig. 11b). This approach can be extended to images with continuously varying intensity distributions; see Sect. 10.

The sub-pixel accuracy of the displacement measurement is affected by the particular image features within the source window; an example is the grid crossing angle which has already been discussed. To address the sub-pixel accuracy using the four corners of a grid intersection, the simulation data from Sect. 4, where the correlation of the entire grid crossing was analyzed, is reprocessed to correlate only the corners instead. Results are shown in Fig. 12 for two intersection angles, Gaussian and non-Gaussian intensity profiles, and different values of S/N . Data from all four corners are included in this figure. The improvement in accuracy with increasing S/N is similar to that shown before for the case of using the complete “X” pattern (see Fig. 5). However, generally a factor of two degradation in absolute accuracy is observed when comparing the corner correlation (Fig. 12) against the whole intersections (Figs. 5 and 6). Also note a slight improvement for non-Gaussian intensity profiles, an observation consistent with the results in Fig. 10. The main conclusion from Fig. 12 is

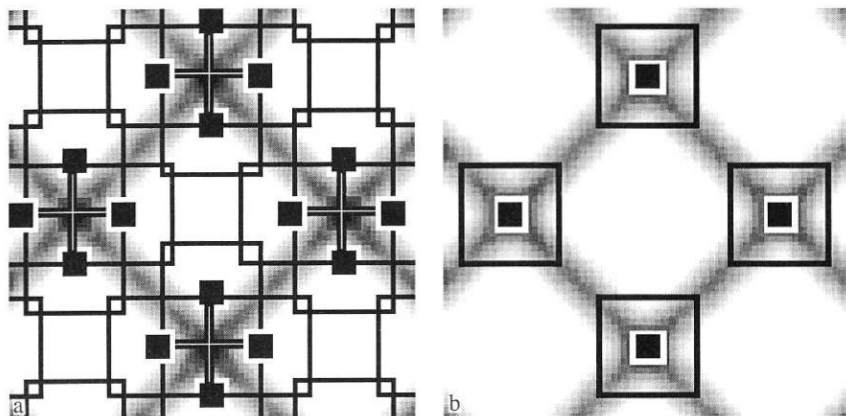


Fig. 11. **a** Source windows located about the four “corners” of a grid intersection; **b** source windows located about the complete grid intersection

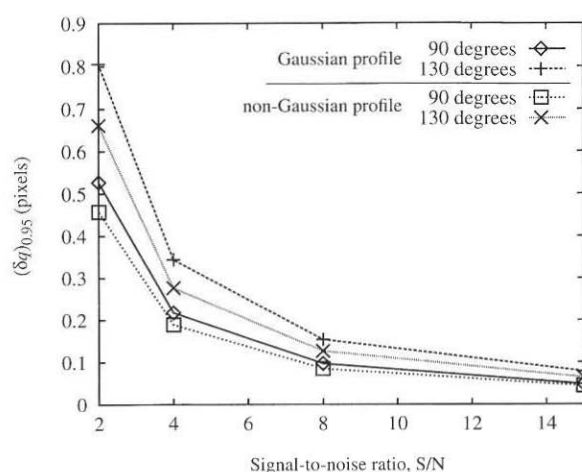


Fig. 12. Displacement sub-pixel accuracy using grid corners versus S/N for two line intensity profiles and grid intersection angles (intensity ratio $R_i = 1$)

that good sub-pixel accuracy is achievable using the corners of an intersection (resulting in the advantages cited above), if the S/N of the image is sufficiently high.

10

Experimental results

Our implementation of molecular tagging diagnostics relies on recently engineered water-soluble molecular complexes with long-lived excited states (i.e., phosphorescence). New findings in molecular recognition and excited state chemistry indicate that mixing certain alcohols with aqueous solutions of a cyclodextrin (CD) cup containing a lumophore results in a phosphorescent complex (Ponce et al. 1993). This triplex alcohol/CD/lumophore complex has a lifetime $\tau \cong 5$ ms. Depending on the placement of the three components of the complex in the flow, we have devised methods for (1) purely velocimetry, (2) molecularly tagging a passive scalar mixing region and monitoring its Lagrangian evolution, and (3) molecularly tagging a chemical reaction interface between two streams and observing its Lagrangian evolution. Only the first two of these implementations are discussed here. The experi-

mental details have been described in the past (Koochesfahani et al. 1993, Gendrich et al. 1994, Koochesfahani et al. 1996).

The experiment involves a vortex ring generated by discharging a slug of fluid from a tube into a reservoir. The phosphorescent complex is premixed with water in the entire flow facility. A pulsed UV laser beam is passed through the appropriate optics to generate an intersecting grid pattern, through which the vortex ring moves (see Fig. 1, for example). The grid pattern is imaged on two CCD cameras synchronized with the laser and with a prescribed time delay between them. The image pairs are digitally acquired by two separate acquisition systems.

The correlation procedure described in this paper has been implemented for the automated processing of time sequences of image pairs. Using a variety of algorithms, the program selects source windows centered on regions with sufficient spatial intensity gradients. The velocity vector field found at one time step is used as a guide for the selection of the roam window at the subsequent time step.

Figure 13 illustrates an individual grid intersection at two different times and the corresponding spatial correlation coefficient field. A well-defined correlation peak is apparent similar to that in the simulations; see Fig. 3. Typical raw velocity data (i.e., no filtering/smoothing) are shown in Fig. 14 in terms of the time evolution of two components of the velocity vector at a point near the axis of symmetry of the passing vortex ring at a station one diameter away from the vortex ring generator. For an ideal vortex ring, at this location in the flow the v -component is expected to remain at zero and the u -component to smoothly increase to a maximum and subsequently drop to zero as the ring passes by. This behavior is captured by the data in Fig. 14. The RMS fluctuation in the v -component data in this figure is determined to be 0.041 pixel corresponding to 0.051 cm/s; 95% of the data fall within ± 0.1 pixel (or ± 0.125 cm/s) of zero. Note that the “noise” in the profiles in this figure includes effects from the experimental setup itself (e.g., a non-ideal vortex ring, potentially non-quiescent reservoir fluid, etc.) as well as the inherent noise in this velocimetry technique as discussed on the basis of our simulations. In spite of all these factors, the noise is within ± 0.1 pixel, consistent with our expectations based on the simulations.

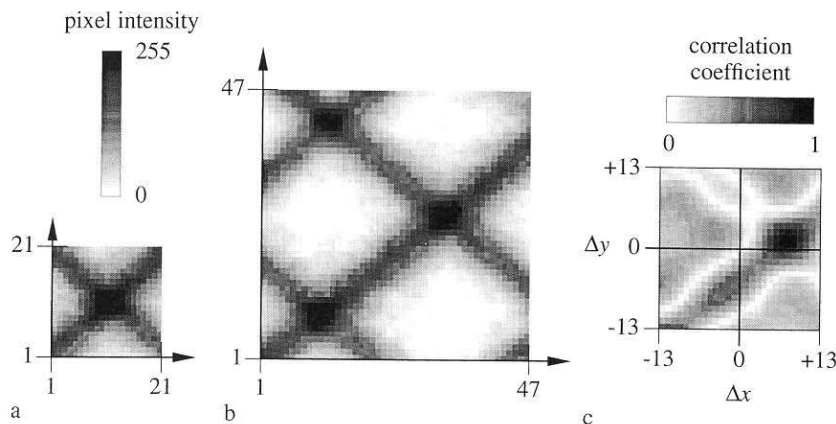


Fig. 13a–c. Experimental grid intersection. a Source window 20 μ s after laser pulse; b roam window from an image of the same molecules 6 ms later; c correlation coefficient field

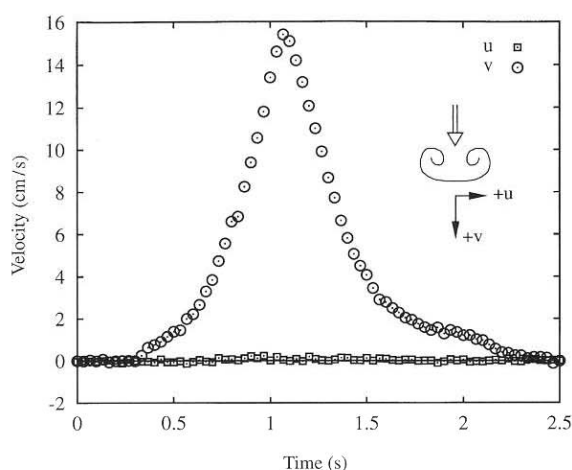


Fig. 14. Time evolution of the u - and v -velocity components measured by MTV near the center of a passing vortex ring

In order to provide an example of tagging a passive scalar mixing region and monitoring its Lagrangian evolution, the alcohol, CD, and lumophore are premixed in the vortex ring fluid, while the reservoir fluid contains only the alcohol solution. The UV laser is arranged to illuminate a series of parallel “bands” in the flow, and the resulting luminescence is imaged on two CCD cameras with a prescribed time delay between them, as before. In Fig. 15a the molecularly tagged patches of the vortex ring fluid at the initial time (20 μ s after

laser firing) are a lighter shade of gray, and the same patches 9 ms later are a darker shade of gray. Only the right half of a downward-moving ring is shown. The velocity vectors at the corners of the patches are determined by the same direct spatial correlation technique described earlier. The velocity vectors in the laboratory frame and in the vortex frame are illustrated in Fig. 15b, c.

As already noted, the purpose of using a grid pattern to illuminate a uniformly seeded flow is to impose an intensity gradient field for the purpose of defining features used in the spatial correlation process. In many turbulent flows the spatially non-uniform scalar concentration field can be used as a natural source of the required luminescence intensity variation. In these cases, laser sheet illumination is sufficient. An example is shown in Fig. 16, illustrating the vortex ring of a starting jet illuminated by a pair crossing UV laser sheets. The placement of the chemical components is the same as that in the vortex ring example of Fig. 15.

Figure 16a is the first image of the tagged flow acquired 20 μ s after the laser firing; the second image, not shown here, is acquired 6 ms later. In a manner similar to that already described, the Lagrangian displacement of small source windows in the first image can be obtained using spatial correlation with the second image. One example of a suitable source window is illustrated in Fig. 16b along with the roam window from the second image in Fig. 16c; the dashed black square indicates where the source window was initially located. The resulting correlation coefficient field indicates a well-defined peak whose pixel coordinates are determined to be $(\Delta x, \Delta y) =$

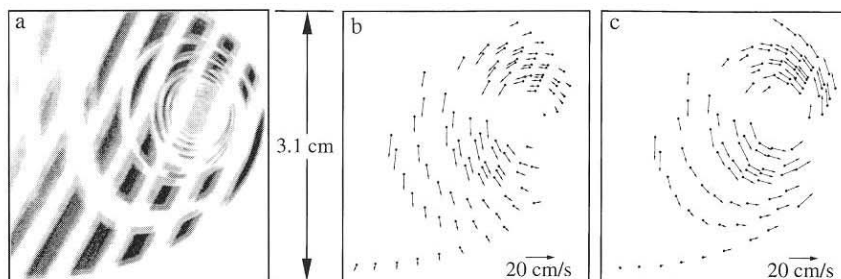


Fig. 15a–c. Lagrangian evolution of molecularly tagged fluid patches in a vortex ring. a Tagged patches at two different times (light grey) 20 μ s and (dark grey) 9 ms; b velocity vectors inferred from a; c velocity vectors with the vortex ring's convection velocity subtracted

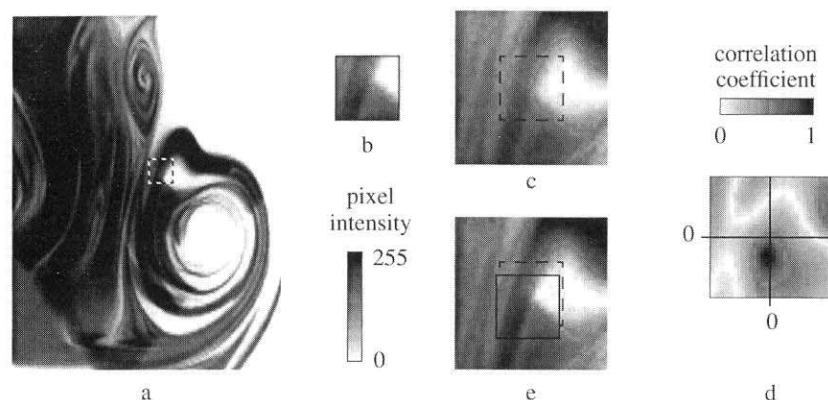


Fig. 16a–e. Correlation technique applied to experimental data from a mixing jet flow field. **a** Earlier image; **b** 21×21 pixel source window from **a**; **c** 51×51 pixel roam window from the second image; **d** correlation coefficient field; **e** superposition of source window over roam window

($-0.9, -5.3$). Figure 16e shows the superposition of **b** over **c**, after **b** has been displaced to the location of peak correlation (the solid black square).

It is implicitly understood that the correlation procedure applied to continuously distributed luminescence fields such as Fig. 16a will yield accurate displacement information in two directions only if sufficient intensity gradients are present within the selected source windows. In areas of the flow where this requirement is not satisfied, a non-uniform laser illumination (e.g., a grid pattern) can be used instead of a laser sheet. We wish to note that the example of Fig. 16 highlights the potential of a molecular tagging approach for simultaneous concentration (from the first image) and velocity (using image pairs) measurements.

11

Conclusions

A spatial correlation approach is presented for determining the Lagrangian displacement field from image pairs based on molecular tagging approaches. The procedure provides significant improvement in measurement accuracy compared to existing approaches for molecular tagging velocimetry (MTV) analysis. Simulations based on grid pattern illumination are performed addressing the effects of a variety of experimental and processing issues on the sub-pixel accuracy of displacement estimates. These issues include the image signal-to-noise ratio and contrast, the grid intersection angle, the order of polynomial used for sub-pixel estimation of displacement, the width of the grid lines, and the size of the correlation source window. Particular experimental implementation difficulties have also been analyzed, such as the effects of non-Gaussian intensity profiles, non-uniform grid intensities, and interlaced versus non-interlaced detection approaches.

The results provide guidelines for optimizing the implementation of MTV. Our results are based on a statistical measure of the accuracy using the 95% confidence interval, which is a much more conservative estimate of accuracy compared to the usually quoted RMS values. It is found that typical accuracies (95% confidence level) of better than 0.1 pixel are readily obtainable. This is an order of magnitude improvement over previous methods used for processing MTV images. The procedure presented is of more general utility for molecular tagging velocimetry than those which require the special case

of a grid pattern illumination; however, the spatial correlation method may lead to a somewhat degraded spatial resolution compared to line-center methods. The contrast is analogous to that between PIV using a group of seed particles versus individual particle tracking. We have successfully applied the spatial correlation method to measure the displacement vector based on the corners of a grid, thereby increasing the density of measurements fourfold, and using features from images of the scalar mixing field. Experimental data in support of this processing technique are provided.

The correlation procedure described here is a first order method for estimating a linear displacement vector; it does not attempt to estimate the higher order derivatives of the velocity field. Within this constraint, the method and the conclusions based on our simulations also apply to processing digital particle image velocimetry (DPIV) image pairs. Our approach can be extended to accommodate the higher order derivatives, for example by taking advantage of advanced direct spatial correlation approaches in DPIV which account for spatial gradients of the velocity field.

References

- Chu CC; Wang CT; Hsieh CS (1993) An experimental investigation of vortex motions near surfaces. *Phys Fluids A* 5: 662
- Falco RE; Chu CC (1987) Measurement of two-dimensional fluid dynamic quantities using a photochromic grid tracing technique. *SPIE* 814: 706
- Falco RE; Nocera DG (1993) Quantitative multipoint measurements and visualization of dense liquid-solid flows using Laser Induced Photochemical Anemometry (LIPA): In: *Particulate Two-Phase Flow* (M. C. Rocco, editor: London). Butterworth-Heinemann, pp. 59–126
- Fincham AM; Spedding GR (1995) Velocity bandwidth, discretization errors and peak-locking phenomena in DPIV measurements. *Bull Am Phys Soc* 40: 2000
- Gendrich CP; Koochesfahani MM; Nocera DG (1994) Analysis of molecular tagging velocimetry images for obtaining simultaneous multi-point velocity vectors. *Bull Am Phys Soc* 39: 1980
- Hill RB; Klewicki JC (1994) Developments and Applications of laser induced photochemical anemometry. *ASME Fluid Eng Div* 191, *Laser Anemometry – 1994: Advances and Applications*, pp 209–216
- Hill RB; Klewicki JC (1996) Data reduction methods for flow tagging velocity measurements. *Exp Fluids* 20: 142
- Huang HT; Fiedler HE; Wang JJ (1993) Limitation and improvement of PIV, Part II: particle image distortion, a novel technique. *Exp Fluids* 15: 263

- Keane RD; Adrian RJ** (1992) Theory of cross-correlation analysis of PIV images. *Appl Sci Res* 49: 191
- Koochesfahani MM; Gendrich CP; Nocera DG** (1993) A new technique for studying the Lagrangian evolution of mixing interfaces in water flows. *Bull Am Phy Soc* 38: 2287
- Koochesfahani MM; Cohn RK; Gendrich CP; Nocera DG** (1996) Molecular tagging diagnostics for the study of kinematics and mixing in liquid phase flows. *Proceedings of the Eighth International Symposium on Applications of Laser Techniques to Fluid Mechanics*, July 8–11, 1996, Lisbon, Portugal
- Lempert WR; Magee K; Ronney P; Gee KR; Haugland RP** (1995) Flow tagging velocimetry in incompressible flow using photo-activated nonintrusive tracking of molecular motion (PHANTOMM). *Exp Fluids* 18: 249
- Maas HG; Stefanidis A; Gruen A** (1994) Feature tracking in 3-D fluid tomography sequences. *First IEEE Int. Conf. on Image Processing*, Austin, Texas, November 13–16, 1994
- Miles R; Cohen C; Conners J; Howard P; Huang S; Markovitz E; Russel G** (1987) Velocity measurements by vibrational tagging and fluorescent probing of oxygen. *Opt Lett* 12: 861
- Ponce A; Wong PA; Way JJ; Nocera DG** (1993) Intense phosphorescence triggered by alcohols upon formation of a cyclodextrin ternary complex. *J Phys Chem* 97: 11137
- Roesgen T; Totaro R** (1995) Two-dimensional on-line particle imaging velocimetry. *Exp Fluids* 19: 188
- Stier B** (1994) An investigation of fluid flow during induction stroke of a water analog model of an IC engine using an innovative optical velocimetry concept – LIPA. PhD Dissertation, Michigan State University
- Tokumaru PT; Dimotakis PE** (1995) Image correlation velocimetry. *Exp Fluids* 19: 1
- Utami T; Blackwelder RF; Ueno T** (1991) A cross-correlation technique for velocity field extraction from particulate visualization. *Exp Fluids* 10: 213